

# ADAPTIVE MORPHOLOGICAL FRAMEWORK FOR 3D DIRECTIONAL FILTERING

TIN BARISIN<sup>✉,1,2</sup>, KATJA SCHLADITZ<sup>2</sup>, CLAUDIA REDENBACH<sup>1</sup> AND MICHAEL GODEHARDT<sup>2</sup>

<sup>1</sup>Image Processing Department, Fraunhofer ITWM, Fraunhofer-Platz 1, 67663 Kaiserslautern, Germany,

<sup>2</sup>Department of Mathematics, University of Kaiserslautern, Gottlieb-Daimler-Straße 47, 67663 Kaiserslautern, Germany

e-mail: tin.barisin@itwm.fraunhofer.de, michael.godehardt@itwm.fraunhofer.de,

katja.schladitz@itwm.fraunhofer.de, redenbach@mathematik.uni-kl.de

(Received November 9, 2021; revised February 2, 2022; accepted March 11, 2022)

## ABSTRACT

Engineering materials often feature lower dimensional and directed structures such as cracks, fibers, or closed facets in foams. The characterization of such structures in 3D is of particular interest in various applications in materials science. In image processing, knowledge of the local structure orientation can be used for structure enhancement, directional filtering, segmentation, or separation of interacting structures. The idea of using banks of directed structuring elements or filters parameterized by a discrete subset of the orientation space is proven to be effective for these tasks in 2D. However, this class of methods is prohibitive in 3D due to the high computational burden of filtering on a sufficiently fine discretization of the unit sphere.

This paper introduces a method for 3D pixel-wise orientation estimation and directional filtering inspired by the idea of adaptive refinement in discretized settings. Furthermore, an operator for distinction between isotropic and anisotropic structures is defined based on our method. This operator utilizes orientation information to successfully preserve structures with one or two dominant dimensions. Finally, feasibility and effectiveness of the method are demonstrated on 3D micro-computed tomography images in three use cases: detection of a misaligned region in a fiber-reinforced polymer, segmentation of cracks in concrete, and separation of facets and strut system in partially closed foams.

Keywords: adaptive directional filtering, computed tomography, crack detection, filter banks, local fiber orientation, local surface normal orientation, orientation estimation.

## INTRODUCTION

In the past few decades, micro-computed tomography ( $\mu$ CT) has gained momentum in materials science and engineering for the purpose of detailed and fully 3D investigation of materials' micro-structures. Materials of interest include concrete, fiber-reinforced materials, foams, woven, and non-woven materials. Characterization of the geometric micro-structure enables understanding and modelling of the material structure and gives a unique insight into the connection of parameters of the production process and the resulting material's properties.

Many materials have a highly anisotropic structure and contain lower dimensional or directed features. In these cases, classical image processing methods such as noise reduction filters should be used carefully to preserve directional information as well as thin lower dimensional features. Moreover, nowadays image sizes well above  $2000^3$  pixels have become common. Therefore, efficient image processing techniques that can handle this massive amount of data are needed.

In 2D, robust smoothing, segmentation, and

analysis of fibrous structures is achieved by rotated anisotropic Gaussian filters whose main axis orientation is evenly sampled on the unit semi-circle (Wirjadi, 2009; Schladitz *et al.*, 2017). The optimal orientation is then chosen pixelwise. However, Wirjadi *et al.* (2016) show that in 3D, this approach becomes computationally too intensive as the number of orientations to be checked to sample as densely as in 2D increases enormously. The idea of filtering using a fine sampling of the orientation space can nevertheless be utilized in 3D. To this end, we reduce the computational burden by checking only a subset of all orientations (Fig. 1). This subset is adapted to the current pixel based on orientation information derived from its local neighbourhood. More precisely, we introduce an adaptive framework for directional filtering and orientation analysis. Our method requires an initial orientation estimation in each pixel to start with. Filtering is then restricted to orientations close to the given initial orientation. This drastically reduces the run-time compared to classical directional filter banks which search the full evenly sampled orientation space.

In 3D, lower dimensional structures may be either linear (1D) or planar (2D). To be able to treat both cases, we use two classes of structuring elements (SEs): line segments and squares.

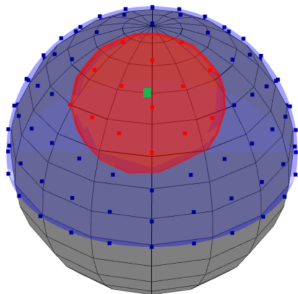


Fig. 1: Example of a search cone (red) around  $(\theta, \varphi) = (2, 2)$  (green, in spherical coordinates, units: radians) on the unit half-sphere (blue). The parameters are  $\delta_{max} = 0.5$  and  $n = 24$  (see Section Discretization of the half-sphere).

We estimate the initial orientation by the established method based on the eigenvectors of the Hessian matrix or more roughly by probing the main directions (main axes, plane, and space diagonals) induced by the pixel grid and choosing one of them. Furthermore, following an idea of Sazak *et al.* (2019), we derive a local structure shape operator by comparing filter responses with varying SE in orthogonal spaces. Finally, we apply our method to three tasks in the analysis of materials structures based on computed tomography (CT): segmenting misaligned regions in a polymer reinforced with long glass fibers, segmentation of cracks in concrete, and facet identification in ceramic foams.

To summarize, we devise a method for fast and yet effective directional filtering in 3D, and an operator for characterizing local structure shape. Both prove to be useful for analyzing materials structures highly relevant in practice.

## RELATED WORK

Our approach combines ideas from two fields of classical image processing: filter steerability or filter banks, and adaptive mathematical morphology. So far, these methods were mostly developed for and applied to 2D images. In 2D, directional filter banks are based on the principle of filtering in a set of orientations evenly-sampled on the unit semi-circle and selecting an orientation based on the maximal/minimal filter response (Freeman and Adelson, 1991; Soille and Talbot, 2001; Michelet *et al.*, 2006; Sandau and Ohser, 2007; Sandberg and Brega, 2007; Schladitz *et al.*, 2017). This class of methods has been applied to

the tasks of filtering, segmentation, and orientation analysis.

In 2D, an even sampling of the unit semi-circle is easily obtained by choosing equidistant points on the interval  $[0, \pi)$ . In 3D, sampling of the unit semi-circle is replaced by sampling on the unit half-sphere (Robb *et al.*, 2007; Sazak *et al.*, 2019; Semeraro *et al.*, 2020). Achieving an even sampling is not a trivial task (Robb *et al.*, 2007; Wirjadi, 2009). Sets of exactly equidistant points on the unit sphere exist only for certain numbers of points (Saff and Kuijlaars, 1997), with the simplest examples being  $N = 2$  and  $N = 6$ . For other numbers of points, sets of approximately equidistant points can be computed using optimization methods. Wirjadi (2009) and Altendorf (2011) provide overviews. Wirjadi (2009) adapted the optimization of Fliege and Maier (1999) to the upper half-sphere, Wirjadi *et al.* (2016) used the same sampling.

Classical mathematical morphology uses fixed SEs for filtering (e.g. dilation, erosion, opening, or closure). Adaptive morphology expands these concepts by varying shape and/or size of the SE in each pixel location depending on local image information. Most common features used for selecting adaptive SEs are local gray value differences (Lerallut *et al.*, 2007; Debayle and Pinoli, 2011), local orientation (Tankyevych *et al.*, 2008; Tankyevych *et al.*, 2009), local structure tensor (Landström and Thurley, 2013), salience (Curic *et al.*, 2012), or local path alignment with the image structure (Heijmans *et al.*, 2005; Luengo Hendriks, 2010; Morard *et al.*, 2014).

Our approach is closely related to the one of Landström and Thurley (2013) who construct elliptical SEs whose axis orientations and sizes are derived from the eigenvectors and eigenvalues of the local structure tensor. Alternatively, directional information can be determined by the analysis of the Hessian matrix in each pixel. The extracted directions have been used for directional line filtering (Tankyevych *et al.*, 2008; Tankyevych *et al.*, 2009), adaptive morphological filtering (erosion or dilation with linear SE) or anisotropic Gaussian filtering for enhancement of linear structures (Su *et al.*, 2014).

Many approaches in adaptive mathematical morphology rely on constructing complex SEs which in 3D result in enormous run-times and require significant computational resources (Dokládál and Dokládálová, 2008). Hence, 3D applications of adaptive morphology are still rare, with a few exceptions (Lerallut *et al.*, 2007; Tankyevych *et al.*, 2009; Luengo Hendriks, 2010).

## MATERIAL AND METHODS

### PRELIMINARIES

Let  $D \subset \mathbb{Z}^3$  be a discrete grid. Then,  $\mathcal{L} = \{I \mid I : D \rightarrow \mathbb{R}^+, x \mapsto I(x) \in \mathbb{R}^+\}$  is the family of all mappings from the grid  $D$  to the real non-negative numbers. An element  $I \in \mathcal{L}$  is called an image.

Most morphological operations and image filters require the choice of a SE (or filter mask). A SE  $B$  is defined as a subset of  $\mathbb{Z}^3$ . Here, we only consider reflection invariant SEs ( $x \in B \iff -x \in B$ ) with  $0 \in B$ , namely line segments and squares. For any pixel (lattice point)  $p \in D$ ,  $B(p) = \{m \in D \mid m - p \in B\}$  refers to a copy of  $B$  translated to the pixel  $p$ . Then, some filter  $\gamma_B : \mathcal{L} \rightarrow \mathcal{L}$  is defined as

$$\gamma_B(I)(p) = \bigotimes \{I(m) \mid m \in B(p)\},$$

where  $\bigotimes$  represents the filtering operation. For instance, computing the mean or median of the gray values yields a mean or median filter while computing the minimum or maximum yields an erosion or dilation, respectively.

Line SEs of a given length can uniquely be parametrized by their orientation. Square SEs will be parametrized by their normal orientation. However, squares are not invariant with respect to rotations around the normal orientation. To obtain a unique parametrization, we choose one of the square's edges to be contained in the intersection of the  $xy$  plane and the plane with the desired normal orientation. The center of the square is then shifted to the origin to ensure reflection invariance. In the special case that the normal orientation is the  $z$  axis, the square is aligned to the  $x$  and  $y$  axes with center in the origin. Line SEs are discretized using the Bresenham (1965) line algorithm. Starting from the center pixel, the line is discretized only in one direction and reflected to ensure symmetry of the SE. Square SEs are constructed by discretizing one of their edges and shifting it along the orthogonal edge.

The unit sphere in  $\mathbb{R}^3$  will be denoted by  $S^2$ . Due to the symmetry of the SEs, orientations on the unit half-sphere  $S^2_+ := \{u = (u_1, u_2, u_3) \in \mathbb{R}^3 : \|u\| = 1, u_3 \geq 0\}$  are sufficient for the parametrization. In practice, only finitely many orientations can be considered which requires an even sampling of the orientations on  $S^2_+$  to avoid introducing systematic errors. We follow the approach of Altendorf (2011) which exploits analogies from the 2D case to compute fast and easily an approximately even sampling on  $S^2_+$  without complicated optimization. The idea is to evenly discretize the unit circle with  $n$  points which

are then projected onto the unit square. Applying this procedure in the three coordinate planes ( $xy$ ,  $yz$ , and  $xz$ ) yields a sampling on the unit cube. The sampling points are then projected on the unit sphere, see Fig. 2, and finally restricted to  $S^2_+$ .

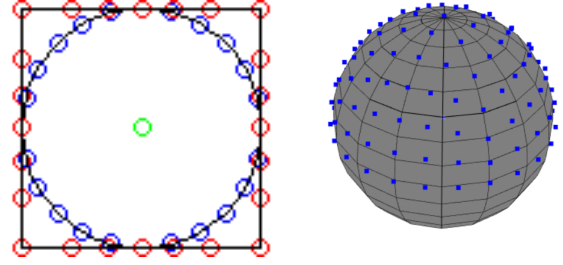


Fig. 2: Discretization of  $S^2_+$  (right) by extrapolation from the unit circle in 2D (left) for  $n = 24$ . Blue dots represent the uniform discretizations of the circle (left) or the sphere (right), while red dots (left) are projections of points from the unit circle to the unit square.

The parameter  $n$  should be a multiple of 8 to ensure that the coordinate axes and diagonals are contained in the sampling. The total number of sampled points on  $S^2_+$  is  $N = n^2/8 + (n/4 + 1)^2$ .

### ESTIMATING INPUT ORIENTATIONS

Our method requires roughly estimated local orientations as input. We suggest two ways to obtain this input.

#### Local orientation from Hessian matrix

An established approach for estimating orientation in 3D images is by analysis of the eigenvalues and eigenvectors of the Hessian matrix (Eberly *et al.*, 1994)

$$H_\sigma = (\nabla^2) (I * g_\sigma), \quad (1)$$

see e.g. Wirjadi *et al.* (2016). Here,  $g_\sigma$  is a Gaussian kernel with standard deviation parameter  $\sigma$ . The parameter  $\sigma$  affects the scale of the observation and should be chosen depending on local structure thickness.

Throughout the paper, the objects of interest will be bright structures on dark background. In this case, the eigenvalues of high absolute value have a negative sign (Frangi *et al.*, 2000). Thus the largest eigenvalue is in fact the smallest in absolute value and vice versa. Hence, the eigenvector of the Hessian matrix  $H_\sigma$  with the largest eigenvalue represents the direction of the smallest change of gray values and is used to estimate the local structure orientation in the image when using a line segment as SE. When using the square SE, we use the eigenvector corresponding to the smallest eigenvalue to estimate the normal direction, as this

vector represents the orientation yielding the strongest change of gray values.

Another established approach for this task is to use the structure tensor (Weickert, 1999; Wirjadi *et al.*, 2016), which is based on the first order derivatives:

$$S_{\sigma,\rho} = g_{\rho} * ((\nabla f * g_{\sigma})(\nabla f * g_{\sigma})),$$

where  $\rho$  is an additional spatial smoothing parameter on the tensor space. The orientation is then estimated from the eigenvectors as done for the Hessian matrix.

### Base axis search

In some cases, local orientation cannot be estimated well via the Hessian matrix, for instance due to poor contrast, noise, imaging artifacts or interaction between structures (as for example in fiber-reinforced materials with high fiber volume fraction). In this case, we consider a small subset of orientations and use the orientation of maximal response as input. For example, the subset consisting of the orientations of the edges, face and space diagonals of the lattice's unit cell yields a test set consisting of 13 orientations (Fig. 3).

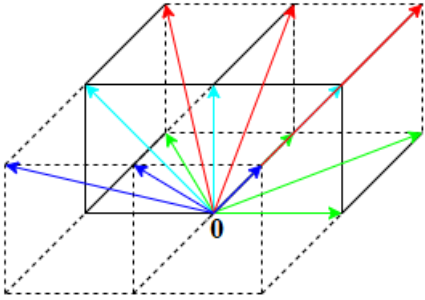


Fig. 3: Base axis search. The 13 orientations from pixel 0 on the upper half-sphere: 4 green in the  $xy$  plane, 3 red in the first diagonal plane, 3 cyan in the  $xz$  plane, 3 blue in the second diagonal plane.

This way of initial orientation estimation may appear rather rough. However, it will be refined and adapted to the local image structure by the subsequent adaptive filtering.

## FRAMEWORK

We aim at efficient and robust directional filtering and orientation estimation in large 3D images. Our main strategy is fine filtering adapted to a given local input orientation. This way, computationally expensive filtering on all sampled orientations can be avoided.

In practice, we assume that each image pixel is assigned a rough estimate of the local orientation of the image content obtained by one of the methods described above. Input images for the adaptive filter are thus an original image  $I \in \mathcal{L}$ , and an image of the

same size as  $I$  containing input orientations  $v(p) \in S_{\pm}^2$  for each pixel  $p \in I$ .

We then consider filter banks with line segment or square SEs that are uniquely parametrized by the line orientation or square normal, respectively. For selecting a subset of filter orientations from the sphere discretization, we define a proximity measure on the parameter space and filter on the much smaller subset of orientations that are close to the given input orientation. Due to the restriction to a subset, we can afford to sample the subspace of the parameter space very finely. This allows to align the SEs precisely to the local image content. We measure proximity by the angular distance between the input orientation in a pixel and the orientations of the SE. That is, for two points  $u, w \in S_{\pm}^2$ , we set

$$d(u, w) = \arccos(|u \cdot w|), \quad (2)$$

where “ $\cdot$ ” denotes standard scalar product.

Let  $S = \{u_1, \dots, u_N\}$  be an even sampling of the unit half-sphere. Then, for every pixel  $p \in I$  with input orientation  $v(p) \in S_{\pm}^2$  we define the search cone as

$$C(p) = \{u \in S : d(u, v(p)) \leq \delta_{max}\},$$

see Fig. 1 for an illustration.

For line or square SEs of half-length  $L$  parametrized by orientation  $u \in S_{\pm}^2$ , the filtering operation is denoted as  $\gamma_{u,SE} : \mathcal{L} \rightarrow \mathcal{L}$ . Here,  $SE \in \{\ell_L, s_L\}$  represents the type of structuring element ( $\ell$  line segment or  $s$  square) used for filtering. For every pixel  $p$  we then report the maximal filter response on its search cone  $C(p)$  and the corresponding orientation by setting

$$\Gamma_{max}^{SE}(I)(p) = \max_{u \in C(p)} [\gamma_{u,SE}(I)(p)], \quad (3)$$

and

$$\Gamma_{arg}^{SE}(I)(p) = \arg \max_{u \in C(p)} [\gamma_{u,SE}(I)(p)]. \quad (4)$$

Note that the correct full notation would be  $\Gamma_{max}^{SE}(I, v)$  for input orientation image  $v : D \rightarrow S_{\pm}^2$ . We restrict to  $\Gamma_{max}^{SE}(I)$  for the sake of easier readability. In summary, parameters of the method are the sampling size  $N$  of the unit (half-)sphere, the bound  $\delta_{max}$  on the angular distance defining the size of the search cone, and the half-length of the SE  $L$  (half edge length in case of a square) measured in the maximum ( $\ell^\infty$ ) norm.

## OPERATOR FOR LOCAL SHAPE CHARACTERIZATION

Identification and characterization of lower dimensional structures is needed in many applications. For example, fibers are locally one-dimensional substructures of the image while cracks are often locally planar. To formalize this, we differentiate three types of structures in 3D images based on their dimension following Frangi *et al.* (2000): blob-like (3D), plate-like (2D), and tubular (1D).

Information on the local dimension or shape can be obtained by comparing filter responses with line and square as SE in orthogonal spaces. To be more precise, in a pixel  $p$ , filter responses of a square filter with normal  $u$  and a line segment filter oriented in  $u$  are compared via

$$R_{aniso}(p) = |[\gamma_{u,\ell_L}(I)](p) - [\gamma_{u,s_L}(I)](p)|. \quad (5)$$

Note that the operator is actually a function of the input image  $I$  and the orientation image, but again we opt for the more compact notation omitting the orientation dependency.

If the structure is isotropic, filter responses in orthogonal directions should be similar and hence  $R_{aniso}(p)$  tends to be low. On the other side, if the structure is anisotropic, filter responses tend to differ because line and plate cannot be fitted to the structure at the same time. Hence, high values of  $R_{aniso}(p)$  indicate local anisotropy.

The orientation  $u = \Gamma_{arg}^{SE}(I)(p)$  is determined by Equation (4) with  $SE$  chosen depending on the goal of the analysis: If  $SE = s$ , then  $R_{aniso}$  distinguishes 2D from 3D structures. If  $SE = \ell$ , then  $R_{aniso}$  differentiates 3D structures on the one hand and 1D/2D structures jointly on the other hand, see Fig. 4 for a toy example.

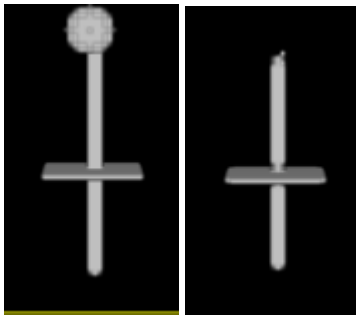


Fig. 4: Example: Removing a 3D ball from a 2D plate and a 1D fiber from a binary image by using the shape operator  $R_{aniso}$  as defined in (5) with  $SE = \ell$  with  $\gamma_{u,\ell_L}$  being a median filter.

Junctions, where two or more oriented structures meet as in Figs. 4 and 8, are hard to classify based on local orientation or anisotropy as the superposition may no longer feature a clearly preferred orientation. Su *et al.* (2014); Altendorf (2011), and Sazak *et al.* (2019) suggest ways to deal with junctions when segmenting vessels. In 2D, Su *et al.* (2014) detect junction points in a post-processing step and handle them by a tailor-suited filter. That results in increased computational burden and run-time. Altendorf (2011) detects junctions, removes them, and finally reconnects fibers based on local orientation. Sazak *et al.* (2019) achieve correct junction handling in 3D, mostly thanks to covering the full sampling space on several scales.

We adapt the operator  $R_{aniso}$  from (5) for improved junction handling as

$$R_{aniso}^*(p) = |\Gamma_{max}^{s_L}(I)(p) - (\Gamma_{max}^{\ell_L}(I^c))^c(p)|, \quad (6)$$

where  $\Gamma_{max}^{\ell_L}(I^c)$  represents filtering with  $SE = \ell$  on  $I^c$  i.e. on the inverted or negative image of  $I$  with  $\Gamma_{arg}^{s_L}(I)$  as an input orientation and  $\delta_{max} = 0.5$ . This operator  $R_{aniso}^*$  is well suited for detecting junctions of locally plate-like structures as in Fig. 8, comes however also at the cost of increased computational effort.

## IMPROVED EFFICIENCY

Here, we argue why our approach is more efficient than filter banks using all evenly sampled points on  $S_{\pm}^2$ . For sampling  $N$  orientations, the filter bank would run  $N$  filters per pixel. For our adaptive filtering, the number of orientations considered per pixel can be approximated by  $\frac{A_{cone}}{A_{sphere}}N$ , where  $A_{cone} = 2\pi(1 - \cos(\delta_{max}))$  is the surface area of the spherical cap representing the search cone (red region in Fig. 1) and  $A_{sphere} = 2\pi$  is the surface area of  $S_{\pm}^2$ . This yields  $(1 - \cos(\delta_{max}))N$  orientations to be considered in each pixel.

For  $\delta_{max} = 0.5$ , that we use throughout the paper, this equals  $0.1224N$ . For the adaptive filtering with base axis search input, 13 additional scans are required for the computation of the initial orientation estimate. Hence, the total number of filtered orientations per pixel equals  $13 + (1 - \cos(\delta_{max}))N$ . This is smaller than  $N$  for all  $N \geq 16$ . Note that according to Wirjadi *et al.* (2016) a sampling with  $N = 98$  is not sufficiently fine for local fiber orientation estimation. Thus, efficiency is significantly improved.

For the case of adaptive filtering with input orientations derived from the Hessian, an explicit

<sup>1</sup>For an image of size  $m_W \cdot m_H \cdot m_D$  voxels. The Gaussian kernel is separable and there are  $O(1)$  per pixel recursive implementations of a 1D Gaussian filter.

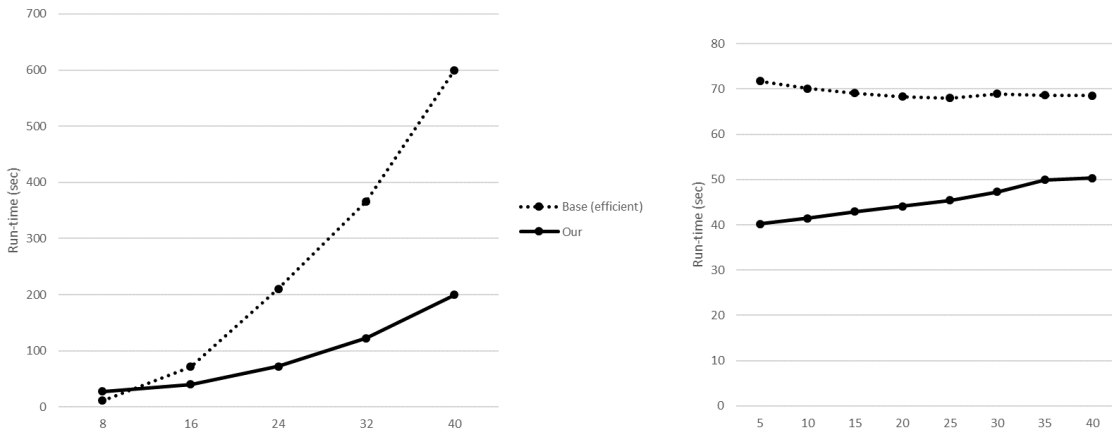


Fig. 5: Run-time analysis for varying parameter configurations on the image from Table 1. Left: varying discretization parameter  $n$  for  $\delta_{max} = 0.5$  and  $L = 5$ , right: varying half-length parameter  $L$  for  $\delta_{max} = 0.5$  and  $n = 16$ . Here, the parameter  $n$  refers to the number of sampled points on the intersection of unit sphere and  $xy$  plane in contrast to the total number of sampled points on the sphere  $N$ , as described in Preliminaries.

formula is harder to find as the complexity of the input orientation estimation is the sum of complexities of Gaussian filtering ( $O(m_W m_H + m_W m_D + m_H m_D)$  complexity<sup>1</sup>), finite difference filters ( $O(m_W \cdot m_H \cdot m_D)$  complexity), and the eigenvalue analysis. In practice, it turned out to be even faster than the base axis search.

Method	Time (s)
Our	45.3
Base	166.7
Base (efficient)	75.5

Table 1: Run-time comparison of our method with brute-force approach and efficient algorithm of Soille and Talbot (2001) for parameters  $L = 5$ ,  $n = 16$ ,  $\delta_{max} = 0.5$ , and  $SE = \ell$  applied to simulated crack image of size  $256^3$ .

Our method is compared with methods for directional line filtering ( $SE = \ell$ ) in all sampled orientations and run-times are given in Table 1 and Fig. 5. Our method could be extended brute force to line filtering in every orientation by setting  $\delta_{max} = \frac{\pi}{2}$ , i.e. by selecting the largest possible search cone. We denote this approach by "Base" in Table 1. However, more efficient implementations of directional filters have been suggested (Soille and Talbot, 2001; Dokladal and Dokladalova, 2008; 2011; Perreault and Hebert, 2007). These implementations exploit periodicity in the SE discretization to achieve linear complexity in image size and constant complexity in the length of the SE. We compare our method to the one of Soille and Talbot (2001), denoted by "Base (efficient)" in Table 1. As expected, our method is more than three times faster than "Base". Furthermore, our method also proves to be faster than "Base (efficient)" for  $L = 5$ . However, for increasing half-length  $L$ , "Base (efficient)" will

eventually become faster than our method due to constant complexity in the half-length  $L$  (Fig. 5 right). Unfortunately, our method cannot be implemented in this way, since each pixel has its own search cone i.e. its own subset of orientations for filtering.

## RESULTS

We now apply the proposed methodology to three types of structures: fibers, cracks, and partially closed foams. Fibers are long, locally cylindrical objects that can be detected using 1D line SEs. Cracks can be seen as 2D surfaces which can locally be captured by a 2D square SEs. Since plate-like cracks have to be distinguished from blob-like pores, our local shape operator is needed. Finally, in ceramic foams, essentially one-dimensional struts and essentially two-dimensional closed walls are intertwined, but shall be analyzed separately.

All run times reported in the following are observed using a machine equipped with an Intel i7-8665U processor running at 1.90 MHz and 16 GB of RAM, running on Linux OS.

### USE CASE 1: MISALIGNED REGION SEGMENTATION IN A GFRP

Glass fiber reinforced polymers (GFRP) are widely used in light-weight construction. Mechanical properties of the material like strength and stiffness are strongly anisotropic depending on the local orientation of the fibers in the material. Therefore, fiber orientation analysis plays an important role in developing fiber reinforced composites and dimensioning parts made

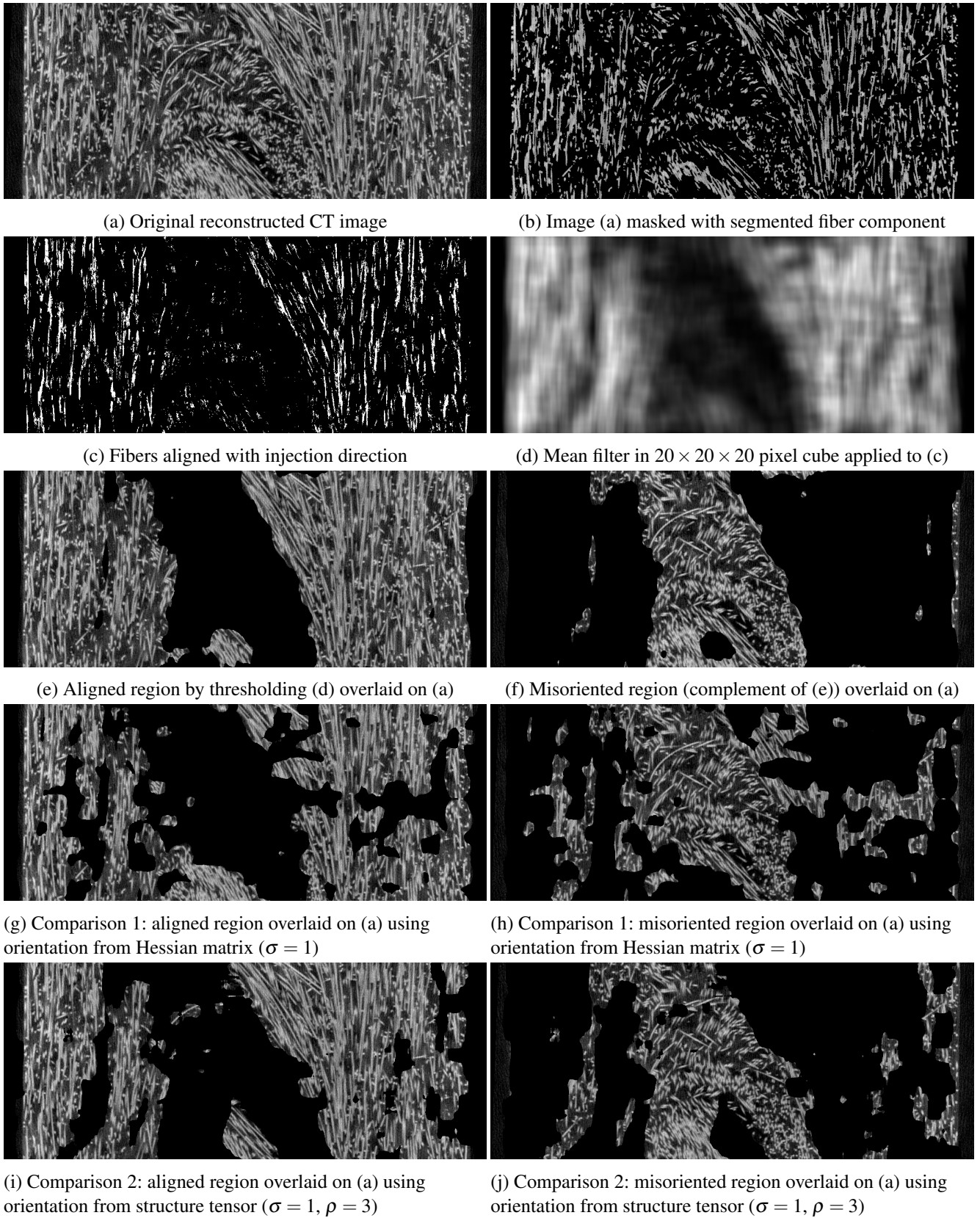


Fig. 6: Use case 1. Misaligned region detection in a long-glass-fiber-reinforced polymer: from left to right, from top to bottom - 2D slice views of the input image, fiber component, fibers following the injection direction, smoothed system of those fibers, region where fibers are aligned, and misaligned region. Slices consist of  $1100 \times 500$  pixels cropped from  $1100 \times 500 \times 200$  pixels with spacing  $4 \mu\text{m}$ .

of them. A common way to produce this type of materials is injection molding. During this process, fibers essentially follow the flow. However, it is well known that fiber orientations deviate in a central layer whose exact characteristics depend on the production parameters. Local fiber orientations can be predicted by numerical simulations, but prediction gets harder with increasing fiber length and fiber volume fraction. Quantifying the misalignment helps to understand how production parameters influence it and to check the quality of flow simulations (Wirjadi *et al.*, 2014).

Procedures for detecting anomaly regions are based either on orientation analysis using the Hessian matrix, see (Dresvyanskiy *et al.*, 2020), or on fiber separation and subsequent analysis of the orientations of these individual fibers. In many cases, single fiber separation is not possible due to sample properties or insufficient resolution. This is a particular problem in materials with high fiber volume fraction, where fibers frequently touch even if the fiber cross-section is sufficiently well resolved. In these cases, Hessian based orientation analysis may be locally unstable. We thus use the base axis search for estimating input orientations.

We reconsider one of the 3D images of GFRP discussed by Wirjadi *et al.* (2014). Samples and CT images are provided by the Leibniz Institute for Composite Materials (IVW) in Kaiserslautern, Germany. We crop a sub-volume of  $1100 \times 500 \times 200$  pixels, see Fig. 6a).

Due to the high fiber volume fraction, fibers cannot be separated completely. Hence, we aim at segmenting the misaligned region based on the estimated orientation  $\Gamma_{arg}^{\ell L}(I)$ . This is achieved through a four step procedure which includes:

1. orientation estimation,
2. separation of the fiber system based on orientation,
3. region detection using the dominant orientation,
4. post-processing.

It demonstrates the abilities of our improved adaptive orientation estimation. Step by step results of the procedure are shown in Fig. 6. Next we describe each step in detail.

In the first step, we apply our method using  $\Gamma_{arg}^{\ell L}(I)$  from (4) with a line SE with parameters  $n = 40$ ,  $L = 20$ ,  $\delta_{max} = 0.5$  using the median filter. This takes 98 minutes. In the second step, the fiber component is segmented. Fiber bundles should provide more stable orientation information than single fibers which may also be outliers. To extract the bundles,

we apply the approach of Sliseris *et al.* (2015) to the image  $\Gamma_{arg}^{\ell L}(I)$ . The method is based on the 2nd order orientation tensor, roughly the 2nd moment of the local orientation, averaged over a small neighborhood, see Wirjadi *et al.* (2016) for details. In fiber pixels, the orientation tensor has one dominant eigenvalue. Hence, the ratio of the largest and the second eigenvalue can be used to select fiber bundles. The result is shown in Fig. 6b).

In the third step, the orientation image  $\Gamma_{arg}^{\ell L}(I)$  is masked with the detected fiber bundles. A dominant orientation and its range are clearly visible from a 2D histogram of the remaining parts of  $\Gamma_{arg}^{\ell L}(I)$  in spherical coordinates which enables separation of the aligned region. That is, pixels whose orientation in spherical coordinates is in the range  $[1.3, 1.7] \times [1.1, 1.9]$  are considered aligned with the dominant orientation (y, thus vertical in the  $xy$  slices shown in Fig. 6c). In a final fourth step, a mean filter with a  $30 \times 30 \times 30$  filter mask (Fig. 6d) and final thresholding yield the aligned and misaligned regions (Figs. 6e and 6f, respectively).

Note that the refined orientation estimation is crucial in this process. To show effectiveness of our method, we use the same four-step procedure with one change: in the first step we plug in the orientation estimation from the established methods. Applying the same framework to the orientation data obtained from the Hessian matrix did not yield convincing results (Figs. 6g and 6h). Using the structure tensor (Weickert, 1999; Wirjadi *et al.*, 2016) instead yields slightly better results (Figs. 6i and 6j). However, single misaligned fibers in the aligned region still cause artifacts, and boundary and shape of the misaligned region remain less smooth and compact compared to the one derived by our approach.

## USE CASE 2: CRACK SEGMENTATION

Concrete is the most used construction material. 3D imaging by  $\mu$ CT enables non-destructive investigation of its internal structure in high resolution. In particular, damage processes and crack formation can be analyzed which is vital for better understanding of the properties of various concrete types and mixtures.

Crack segmentation in 3D images of concrete is challenging due to: (i) cracks being thin structures of varying shape and thickness, and (ii) concrete being a highly heterogeneous material with a variety of sub-types and components (e.g. pores, cement matrix, larger gravel, reinforcement structures). In CT images, cracks can be distinguished from most other structure components by means of their low gray value. However, cracks and pores, both being

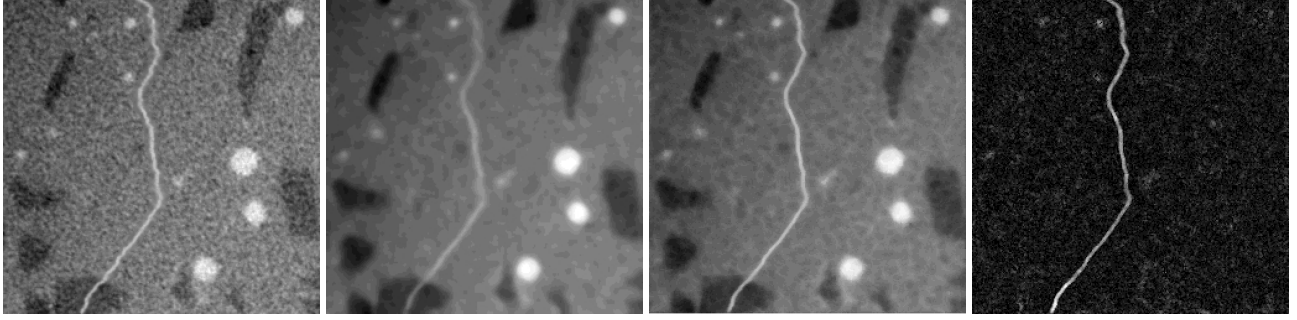


Fig. 7: Use case 2. 2D slice views of crack detection by adaptive square filtering: input image  $I$  (inverted version of the original image), standard median filter with  $7 \times 7 \times 7$  mask (for comparison),  $\Gamma_{max}^{SL}(I)$ , and  $R_{aniso}$  (from left to right). The image consists of  $256 \times 256 \times 256$  pixels with spacing  $37.83 \mu\text{m}$ .

filled with air, appear typically similarly dark. Hence, distinguishing both components requires additional local shape characterization. We perceive cracks to be 2D structures being thin compared to other concrete components. For their segmentation, we apply our operator  $R_{aniso}$  from (5) with input orientation  $v = \Gamma_{arg}^{SL}(I)$  computed on the inverted image. Crack structures will have high values of  $R_{aniso}$  such that they can successfully be distinguished from ball-shaped pores by simple thresholding.

We test our method on a  $256 \times 256 \times 256$  pixel simulated crack image. The concrete background is derived from a sample provided by the Department of Civil Engineering, University of Kaiserslautern, and scanned at Fraunhofer ITWM with a pixel edge length of  $37.83 \mu\text{m}$ . For details on the crack simulation and image synthesis, we refer to Barisin *et al.* (2021).

Results are shown in Fig. 7 for the parameters  $n = 16$ ,  $L = 3$ , and  $\delta_{max} = 0.5$  using the median filter on a square. The initial orientations are estimated from the Hessian matrix. The adaptive filtering using the input orientation from the Hessian matrix takes 57 seconds. For comparison, we also show the original image filtered by a  $7 \times 7 \times 7$  median filter, i. e. the edge length of the filter mask is equal to the SE edge length. Both filters reduce noise. The  $7 \times 7 \times 7$  median filter blurs the crack and reduces the contrast. Our filter  $\Gamma_{max}^{SL}(I)$  is able to enhance the crack structure while reducing background noise at the same time. Additionally,  $R_{aniso}^*$  allows for a better handling of crack junctions than  $R_{aniso}$ , see Fig. 8.

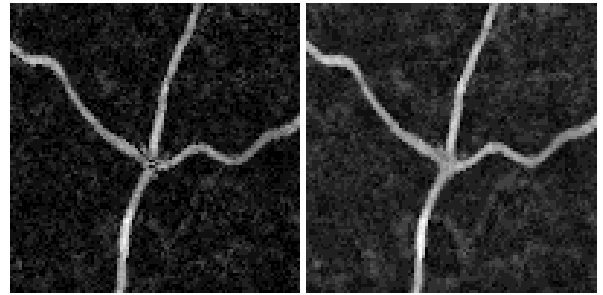


Fig. 8: Use case 2. Junction analysis on 3D crack image:  $R_{aniso}$  (left) and  $R_{aniso}^*$  (right).

For the final segmentation, we threshold the output of  $R_{aniso}^*$  with lower and higher thresholds and use the results as mask and marker image, respectively, in a morphological reconstruction by dilation according to Soille (1999). The higher threshold extracts just the crack centerline, while the lower threshold extracts the full crack structure. The morphological reconstruction reduces noise and ensures extraction of the crack as a connected component.

	Single crack			Junctions		
	P	R	F1	P	R	F1
$R_{aniso}$	0.78	0.83	<b>0.79</b>	<b>0.84</b>	0.80	0.82
$R_{aniso}^*$	0.73	<b>0.84</b>	0.77	0.83	0.84	<b>0.83</b>
FF	<b>0.80</b>	0.79	0.76	0.78	<b>0.87</b>	0.82
TM	0.78	0.76	0.76	0.80	0.74	0.77

Table 2: Quantitative comparison of operators  $R_{aniso}$  and  $R_{aniso}^*$  with Frangi filter (FF) and template matching (TM).

Since the crack was simulated, there exists an unambiguous ground truth to compare our thresholded and post-processed result with (Fig. 9). Overall, the crack structure is well captured in the segmentation, albeit being slightly smoothed. The boundary regions of pores being erroneously segmented as crack can be removed by post-processing. Note that the morphological reconstruction improves crack

coverage compared to the simple thresholding applied earlier (Barisin *et al.* (2021)).

Table 2 provides further quantitative analysis and comparison with related methods. The methods are tested on two sets of simulated cracks: a single crack and cracks with junctions. Each set has five samples. Average values of Precision (P), Recall (R, true positive rate), and F1 score are reported for a fixed parameter configuration. Precision denotes fraction of predicted crack pixels that are correctly detected, while Recall describes coverage fraction of the ground truth. F1 is the harmonic mean of precision and recall. More details on these metrics and a more extensive quantitative study are provided by Barisin *et al.* (2021). For all methods, the final segmentation is derived by morphological reconstruction as described earlier. The Frangi filter (Frangi *et al.*, 2000) and template matching as devised by Ehrig *et al.* (2011) are compared with  $R_{aniso}$  and  $R_{aniso}^*$ . Our methods give slightly higher average F1 scores for both the single crack and the crack junctions samples. Our operator  $R_{aniso}^*$ , designed to improve junction handling, gives higher recall values than  $R_{aniso}$  on the crack junctions samples (Fig. 8).

### USE CASE 3: PARTIALLY CLOSED FOAMS

Ceramic foams are routinely used to filter metal melts. They are produced by covering an open cell polymer foam template by a ceramic slurry. The resulting structure can be decomposed into struts and two-dimensional walls. The latter are formed when facets of the open cells of the polymer foam are closed by the slurry. Closed windows in foams affect the permeability. The walls are preferably parallel to the direction in which the polymer foam is squeezed when wetting it with the slurry. Detection and orientation analysis of closed facets enables realistic modelling of foam structures (Redenbach *et al.*, 2008; 2011; Kampf *et al.*, 2015) and the impact of closed windows on permeability (Föhst *et al.*, 2021).

Our operator  $R_{aniso}$  from (5) with input orientation  $v = \Gamma_{arg}^{SL}(I)$  is applied to simulated 3D ceramic foams with partially closed facets generated by Redenbach *et al.* (2011) (referred to as Example 1). The foam is simulated by the strut system of a Laguerre tessellation and some closed facets of the tessellation to create the walls. This results in a foam system whose struts and closed facets have thickness 1. Locally adaptable dilation then yields a realistic foam structure with variable thickness of struts and facets (Fig. 11). This simulated data provides a precise ground truth for validation of our approach. Both, the varying structure

thickness and the smooth transition between struts and walls make the separation challenging, see Fig. 10. We expect our framework to be most effective in the central part of the facet since this is where the planar structure is most pronounced.

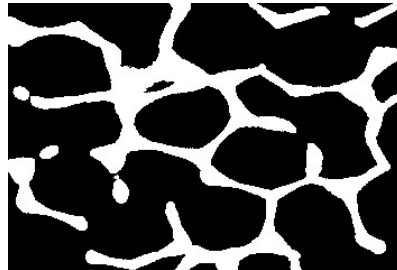


Fig. 10: Use case 3, Example 1. Zoomed in 2D slice view of the simulated ceramic foam structure: no clearly perceivable boundary between facets and struts.

Our framework is applied with square SE and parameters  $n = 24$ ,  $L = 10$ , and  $\delta_{max} = 0.5$  using the mean filter on the SE. The run time is  $\sim 30$  minutes on an image of size  $670 \times 670 \times 270$  pixels. Furthermore, the operator  $R_{aniso}$  is used to distinguish between closed facets and struts. Afterwards, the segmented facet system is post-processed by applying  $\Gamma_{max}^{SL}$  using the median filter to refine detection and remove artifacts.

The segmentation results together with the ground truth are shown in Fig. 12. 3D renderings of the results can be found in Fig. 13. Visually, no obviously misclassified facets can be observed. The segmented strut system covers 75% of the pixels in the strut ground truth. If we introduce an error tolerance by dilating the segmented strut system by 1 pixel, coverage further improves to 93.9%. Since each facet’s medial surface is known, we can calculate the percentage of the facets that was at least partially detected. Approximately 89% of the facets are recognized by our framework. Small and thick facets are the hardest to detect and are often confused with struts even in the eye of the observer. Additionally, the location of the precise boundary between the facets and the struts is highly subjective. Nevertheless, both the coverage percentages and the visual evaluation prove that our framework gives reliable and satisfactory results.

Finally, our framework is applied to a CT image of a real silicon carbide foam. The sample was scanned at Fraunhofer ITWM with pixel edge length  $33.91 \mu\text{m}$  (referred to as Example 2). Further details are described by Kampf *et al.* (2015). On the sub-volume of  $500 \times 500 \times 100$  pixels, our algorithm takes 9.5 minutes. Results are shown in Fig. 14. In this case, no ground truth is available. Hence, the results can only

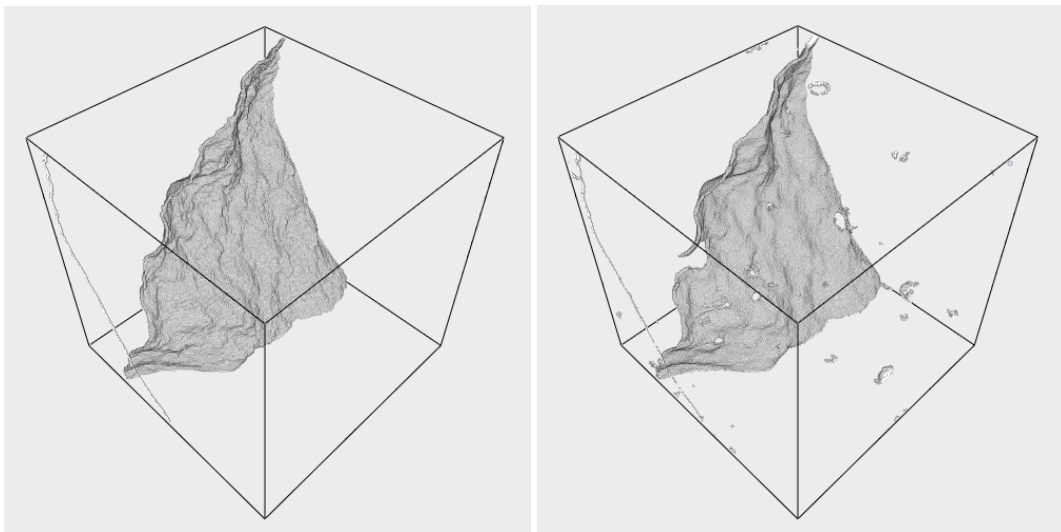


Fig. 9: Use case 2. 3D renderings of the crack segmentation: ground truth and crack obtained by thresholding the post-processed local  $R_{aniso}$ . The image consists of  $256 \times 256 \times 256$  pixels with spacing  $37.83 \mu\text{m}$ .

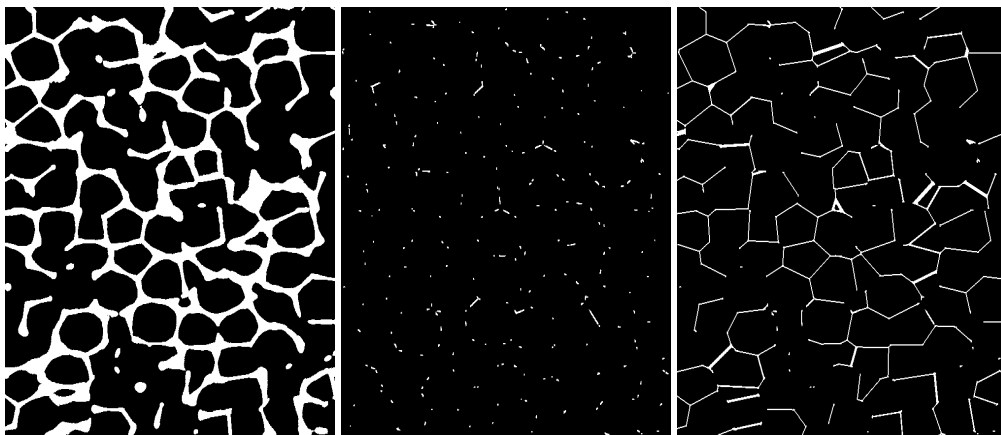


Fig. 11: Use case 3, Example 1. 2D slice views of the ground truth from left to right: simulated foam, strut system, facet system.

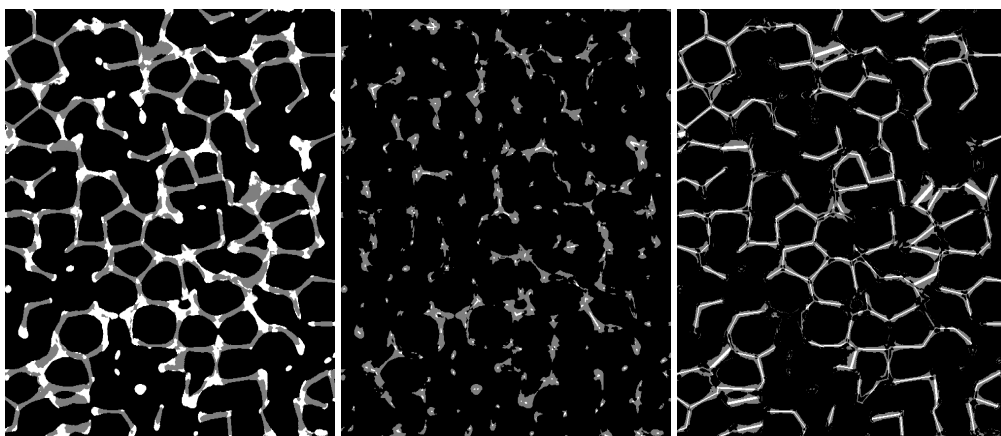


Fig. 12: Use case 3, Example 1. 2D slice views of results. From left to right: separated facets and struts (white - struts, gray - facets), struts overlap with ground truth, and facets overlap with ground truth (for the last two images: white - overlap, gray - difference).

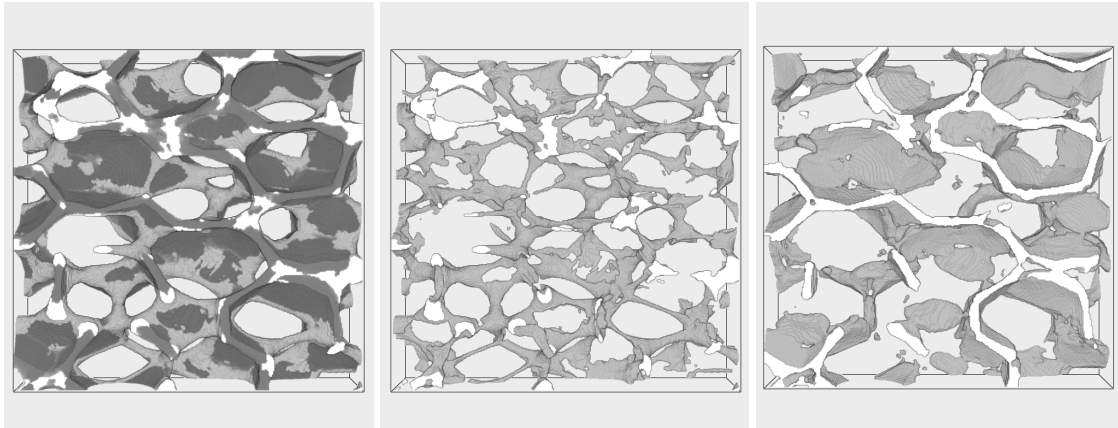


Fig. 13: Use case 3, Example 1. Rendered results for the simulated foam: original image (white - struts, gray - facets), strut system, and facet system.

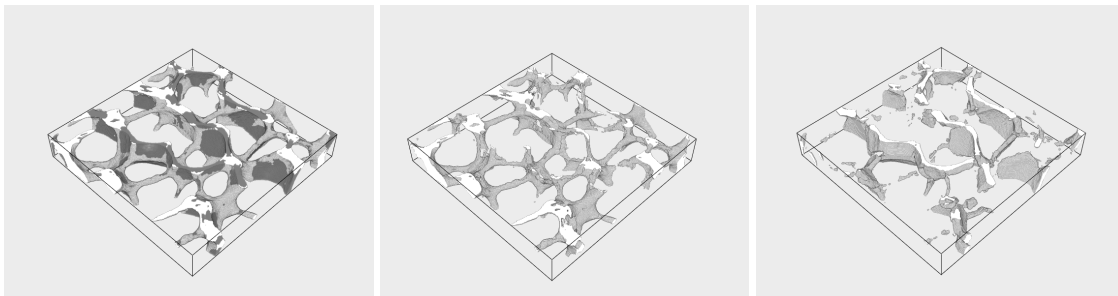


Fig. 14: Use case 3, Example 2. Rendered results for the real ceramic foam: original image (white - struts, gray - facets), strut system, and facet system. The rendered sub-image consists of  $400 \times 400 \times 50$  pixels with spacing  $33.91 \mu\text{m}$ .

be evaluated visually. The segmented wall systems contains some strut pixels. The majority of the walls is however segmented correctly.

## DISCUSSION

We have presented a framework for adaptive directional filtering of 3D image data. The restriction of filter orientations to a cone centered in an initial input orientation avoids checking the full sampled orientation space. That results in significant run-time savings compared to previously suggested methods.

Our algorithm has three main parameters: the half-length  $L$  of the SE, the opening angle of the cone  $\delta_{max}$ , and the sphere discretization parameter  $n$ . The half-length parameter  $L$  depends strongly on the application. It has to approximate the size of the object of interest to be effective. The parameters  $\delta_{max}$  and  $n$  balance run-time and accuracy. The SE size  $L$  limits the discretization density  $n$  since the number of discrete SEs of half-length  $L$  is restricted. For example, there are only 13 discretized lines with half-length 1 in the  $\ell_\infty$  norm (base axis, plane diagonals, space diagonals).

Our method requires a map of input orientations at which the cone is centered. These have to be close to the correct orientation, but do not have to fit it very well. The adaptive filter on the search cone is in fact able to fix imprecision in input orientations or scale and finds the most appropriate orientation. This makes the method more robust and less dependent on the scale parameter  $\sigma$  than classical Hessian directional filtering (Tankyevych *et al.*, 2009).

Our framework is very flexible, can be adapted to specific tasks, and used as building block for various image processing pipelines. This is in particular demonstrated by the adaption of  $R_{aniso}$  to  $R_{aniso}^*$  for handling of crossing cracks.

We have validated our framework in use cases from materials science, it is however not restricted to that area. In biomedical applications, Sandberg and Brega (2007); Tankyevych *et al.* (2008); Tankyevych *et al.* (2009) have used approaches similar to ours but with line SE exclusively. Our algorithm can enhance and extract vessels straightforwardly, too.

## CONCLUSION

We introduced a robust, flexible, and multi-functional method for filtering, enhancement, and separation of oriented structures in 3D. The two outputs – orientation information and filtered image – can be used to solve multiple tasks. We have validated our approach in three use cases for three types of material confirming the wide applicability of the framework. The main benefit of the method is the efficient use of computational resources and decreased run-time compared to directional filters in 3D sampling the complete upper unit half-sphere.

Future work will explore more complex SEs while preserving computational efficiency. Another topic of further research is a thresholding method for precise and reliable unsupervised segmentation of cracks based on  $\Gamma_{max}^{SE}(I)$  from (3) and  $R_{aniso}^*$  from (6).

## ACKNOWLEDGEMENTS

This work was supported by the German Federal Ministry of Education and Research (BMBF) under grant 05M2020 (DAnoBi).

We thank Franz Schreiber at Fraunhofer ITWM (Kaiserslautern, Germany) for scanning the materials and continuous support, the Leibniz Institute for Composite Materials (IVW) in Kaiserslautern, Germany, for providing the glass fiber reinforced polymer data set, and the Department of Civil Engineering from the University of Kaiserslautern, Germany, for providing the concrete sample.

## CONFLICT OF INTEREST

The authors declare that they have no conflict of interest.

## REFERENCES

- Altendorf H (2011). 3D morphological analysis and modeling of random fiber networks: applied on glass fiber reinforced composites. Ph.D. thesis, Technische Universität Kaiserslautern and Mines ParisTech. <http://nbn-resolving.de/urn:nbn:de:hbz:386-kluedo-28323> (accessed 27 July 2021).
- Barisin T, Jung C, Müsebeck F, Redenbach C, Schladitz K (2021). Methods for segmenting cracks in 3d images of concrete: A comparison based on semi-synthetic images. submitted <https://arxiv.org/abs/2112.09493>.
- Bresenham JE (1965). Algorithm for computer control of a digital plotter. *IBM Systems Journal* 4:25–30. <https://doi.org/10.1147/sj.41.0025>.
- Curic V, Luengo Hendriks C, Borgfors G (2012). Saliency adaptive structuring elements. *IEEE J Sel Top Signa* 6:809–19. <https://doi.org/10.1109/JSTSP.2012.2207371>.
- Debayle J, Pinoli JC (2011). Spatially adaptive morphological image filtering using intrinsic structuring elements. *Image Anal Stereol* 24:145–58. <https://doi.org/10.5566/ias.v24.p145-158>.
- Dokladal P, Dokladalova E (2008). Grey-scale 1-d dilations with spatially-variant structuring elements in linear time. In: *EUSIPCO'08*. <https://hal-upec-upem.archives-ouvertes.fr/hal-00622464>.
- Dokladal P, Dokladalova E (2011). Computationally efficient, one-pass algorithm for morphological filters. *J Vis Commun Image R* 22:411–20. <https://doi.org/10.1016/j.jvcir.2011.03.005>.
- Dokládal P, Dokládalova E (2008). Grey-scale morphology with spatially-variant rectangles in linear time. In: *Lect Notes Comput Sc*. [https://doi.org/10.1007/978-3-540-88458-3\\_61](https://doi.org/10.1007/978-3-540-88458-3_61).
- Dresvyanskiy D, Karaseva T, Makogin V, Mitrofanov S, Redenbach C, Spodarev E (2020). Detecting anomalies in fibre systems using 3-dimensional image data. *Stat Comput* 30:1–21. <https://doi.org/10.1007/s11222-020-09921-1>.
- Eberly D, Gardner R, Morse B, Pizer S, Scharlach C (1994). Ridges for image analysis. *J Math Imaging Vis* 4:353–73. <https://doi.org/10.1007/BF01262402>.
- Ehrig K, Goebbels J, Meinel D, Paetsch O, Prohaska S, Zobel V (2011). Comparison of Crack Detection Methods for Analyzing Damage Processes in Concrete with Computed Tomography. In: *Int. Symp. Dig. Ind. Radiol. Comp. Tomogr*. <https://www.ndt.net/article/dir2011/papers/p2.pdf>.
- Fliege J, Maier U (1999). The distribution of points on the sphere and corresponding cubature formulae. *IMA Journal of Numerical Analysis* 19:317–34. <https://doi.org/10.1093/imanum/19.2.317>.
- Föhst S, Osterroth S, Arnold F, Redenbach C (2021). Influence of geometry modifications on the

- permeability of open-cell foams. *AICHE Journal* <https://doi.org/10.1002/aic.17446>.
- Frangi R, Niessen W, Vincken K, Viergever M (2000). Multiscale vessel enhancement filtering. *Med Image Comput Comput Assist Interv* 1496:130–7. <https://doi.org/10.1007/BFb0056195>.
- Freeman WT, Adelson EH (1991). The design and use of steerable filters. *IEEE T Patter Anal* 13:891–906. <https://doi.org/10.1109/34.93808>.
- Heijmans H, Buckley M, Talbot H (2005). Path openings and closings. *J Math Imaging Vis* 22:107–19. <https://doi.org/10.1007/s10851-005-4885-3>.
- Kampf J, Schlachter AL, Redenbach C, Liebscher A (2015). Segmentation, statistical analysis, and modelling of the wall system in ceramic foams. *Mater Charact* 99:38–46. <https://doi.org/10.1016/j.matchar.2014.11.008>.
- Landström A, Thurley MJ (2013). Adaptive morphology using tensor-based elliptical structuring elements. *Pattern Recong Lett* 34:1416–22. <https://doi.org/10.1016/j.patrec.2013.05.003>.
- Lerallut R, Decenci re  , Meyer F (2007). Image filtering using morphological amoebas. *Image and Vision Computing* 25:395–404. *Lect Notes Comput Sc*, <https://doi.org/10.1016/j.imavis.2006.04.018>.
- Luengo Hendriks CL (2010). Constrained and dimensionality-independent path openings. *IEEE T Image Process* 19:1587–95. <https://doi.org/10.1109/TIP.2010.2044959>.
- Michelet F, Da Costa JP, Baylou P, Germain C (2006). Local orientation estimation in corrupted images. In: Zheng N, Jiang X, Lan X, eds., *Lect Notes Comput Sc*. Berlin, Heidelberg: Springer Berlin Heidelberg. [https://doi.org/10.1007/11821045\\_37](https://doi.org/10.1007/11821045_37).
- Morard V, Dokl dal P, Decenci re   (2014). Parsimonious path openings and closings. *IEEE T Image Process* 23:1543–55. <https://doi.org/10.1109/TIP.2014.2303647>.
- Perreault S, Hebert P (2007). Median filtering in constant time. *IEEE T Image Process* 16:2389–94. <https://doi.org/10.1109/TIP.2007.902329>.
- Redenbach C, Giertsch M, Godehardt M, Schladitz K (2008). Modelling a ceramic foam using locally adaptable morphology. *J Microsc Oxford* 230:396–404. <https://doi.org/10.1111/j.1365-2818.2008.01998.x>.
- Redenbach C, Wirjadi O, Rief S, Wiegmann A (2011). Modeling of ceramic foams for filtration simulation. *Adv Eng Mater* 13:171–177. <https://doi.org/10.1002/adem.201000222>.
- Robb K, Wirjadi O, Schladitz K (2007). Fiber orientation estimation from 3d image data: Practical algorithms, visualization, and interpretation. In: *Proc. 7th Int. Conf. Hybrid Intelligent Systems*. Kaiserslautern, Germany. <https://doi.org/10.1109/HIS.2007.26>.
- Saff E, Kuijlaars A (1997). Distributing many points on a sphere. *Mat Intel* 19:5–11. <https://doi.org/10.1007/BF03024331>.
- Sandau K, Ohser J (2007). The chord length transform and the segmentation of crossing fibres. *J Microsc Oxford* 226:43–53. <https://doi.org/10.1111/j.1365-2966.2007.01748.x>.
- Sandberg K, Brega M (2007). Segmentation of thin structures in electron micrographs using orientation fields. *J Struct Biol* 157:403–15. <https://doi.org/10.1016/j.jsb.2006.09.007>.
- Sazak C, Nelson CJ, Obara B (2019). The multiscale bowler-hat transform for blood vessel enhancement in retinal images. *Patter Recogn* 88:739–50. <https://doi.org/10.1016/j.patcog.2018.10.011>.
- Schladitz K, B ter A, Godehardt M, Wirjadi O, Fleckenstein J, Gerster T, Hassler U, Jaschek K, Maisl M, Maisl U, Mohr S, Netzelmann U, Potyra T, Steinhauser MO (2017). Non-destructive characterization of fiber orientation in reinforced smc as input for simulation based design. *Compos Struct* 160:195–203. <https://doi.org/10.1016/j.compstruct.2016.10.019>.
- Semeraro F, Ferguson JC, Panerai F, King RJ, Mansour NN (2020). Anisotropic analysis of fibrous and woven materials part 1: Estimation of local orientation. *Comp Mater Sci* 178:109631. <https://doi.org/10.1016/j.commatsci.2020.109631>.
- Sliseris J, Andr  H, Kabel M, Wirjadi O, Dix B, Plinke B (2015). Estimation of fiber orientation and fiber bundles of MDF. *Mater Struct* 49. <https://doi.org/10.1617/s11527-015-0769-1>.
- Soille P (1999). *Morphological Image Analysis: Principles and Applications*. Berlin, Heidelberg: Springer. <https://doi.org/10.1007/978-3-662-03939-7>.

- Soille P, Talbot H (2001). Directional morphological filtering. *IEEE T Patter Anal* 23:1313–29. <https://doi.org/10.1109/34.969120>.
- Su R, Sun C, Zhang C, Pham TD (2014). A new method for linear feature and junction enhancement in 2d images based on morphological operation, oriented anisotropic gaussian function and hessian information. *Pattern Recogn* 47:3193–208. <https://doi.org/10.1016/j.patcog.2014.04.024>.
- Tankyevych O, Talbot H, Dokládál P (2008). Curvilinear morpho-hessian filter. In: 2008 I S Biomed Imaging. <https://doi.org/10.1109/ISBI.2008.4541170>.
- Tankyevych O, Talbot H, Dokládál P, Passat N (2009). Direction-adaptive grey-level morphology. application to 3d vascular brain imaging. In: *IEEE Image Proc*. <https://doi.org/10.1109/ICIP.2009.5414356>.
- Weickert J (1999). Coherence-enhancing diffusion filtering. *Int J Comput Vis* 31:111–27. <https://doi.org/10.1023/A:1008009714131>.
- Wirjadi O (2009). Models and Algorithms for Image-Based Analysis of Microstructures. Ph.D. thesis, Technische Universität Kaiserslautern. <https://kluedo.ub.uni-kl.de/frontdoor/index/index/year/2009/docId/2077> (accessed 27 July 2021).
- Wirjadi O, Godehardt M, Schladitz K, Wagner B, Rack A, Gurka M, Nissle S, Noll A (2014). Characterization of multilayer structures in fiber reinforced polymer employing synchrotron and laboratory X-ray CT. *Int J Mater Res* 105:645–54. <https://doi.org/doi:10.3139/146.111082>.
- Wirjadi O, Schladitz K, Easwaran P, Ohser J (2016). Estimating fibre direction distributions of reinforced composites from tomographic images. *Image Anal Stereol* 35:167–79. <https://doi.org/10.5566/ias.1489>.